Setting robust manufacturing tolerances for turbine trailing edge film cooling

Tassilo von Mueller*

Dept. of Engineering Science,
University of Oxford
Oxford, OX1 3PJ, United Kingdom
Email: tassilo.vonmueller@eng.ox.ac.uk

Peter Ireland
Dept. of Engineering Science,
University of Oxford
Oxford, OX1 3PJ, United Kingdom

Dougal Jackson
Rolls-Royce PLC
Derby DE24 8BJ, UK

ABSTRACT

The trailing edge of a high-pressure turbine blade presents a challenge to turbine cooling engineers. Its thin nature requires that film cooling holes are manufactured through electrode discharge machining (EDM), a process which requires high precision in order to prevent extreme variations in hole geometry and location. Previous studies on manufacturing tolerances have looked at fan-shaped holes and only on flat plates. This study[1] *aims to understand the extremes of possible manufacturing variations in the trailing edge cutback region of a high pressure turbine blade to help set appropriate manufacturing limits. A row of cylindrical film holes with a radial inclination of 30° was tested and used as the benchmark. Several film hole configurations were then tested over a range of blowing ratios. These included film hole shifts between cutback section and ejection plane as well as cutback step shifts, resulting in a change in the thickness of the cutback thickness. The experiments were carried out in the high velocity 2D linear cascade experimental facility*

*Corresponding author
[1]This study was presented at Turbo Expo 2025 under GT2025-152251

using pressure sensitive paint (PSP) to measure film effectiveness. At low blowing ratios, most manufacturing variations were found to have very little effect on film cooling effectiveness. At higher blowing ratios, higher offsets between the cutback section and the film hole ejection plane were found to have greater detrimental effects on film cooling effectiveness. A numerical study was completed to complement the experimental findings and support the understanding of manufacturing limits in trailing edge film holes.

NOMENCLATURE

A Area

BR Blowing Ratio

D Diameter

DR Density Ratio

EDM Electrode Discharge Machining

FP Flow Parameter, $\dot{m}\sqrt{T_c}/(P_c A_c)$

K Kelvin

k Thermal Conductivity [W/m·K]

LHS Large Hole Shift

Ma Mach number

$\dot{m}$ Mass flow rate

NS Negative step shift

PR Pressure Ratio

PS Positive Step Shift

PSP Pressure Sensitive Paint

R Radius of Curvature

RS Rounded Step

SHS Small Hole Shift

TE Trailing Edge

u Flow Velocity

W Molecular Weight

w^+ Non-Dimensional Mass Flow Rate

x Streamwise Distance

y Vertical Distance

z Spanwise Distance

η_f Adiabatic Film Effectiveness

η_c Cooling Efficiency

ϵ Cooling Effectiveness

γ Effective Injection Angle

ρ Fluid Density

air Air

b Black

c Coolant

f Film

∞ Mainstream

m Metal

ref Reference

s Static

0 Total

Keywords: Trailing Edge, Film cooling, Pressure Sensitive Paint

1 INTRODUCTION

The trailing edge of a high pressure turbine blade represents a challenging region for turbine blade manufacturers. In order to minimise aerodynamic losses, the trailing edge needs to be tapered with minimal thickness. However, the harsh environment causes high thermal and mechanical stresses within that region. Modern gas turbine manufacturers are continually attempting to increase the thermal efficiency of gas turbines. This process has caused turbine entry temperatures to exceed the material properties of most turbine components. To prevent a breakdown of

parts, film cooling is widely used in order to reduce metal temperature and thereby increase the longevity of turbine blades. Coolant air is taken from the compressor and bled through film holes to create a layer of cold air between the hot combustion gases and the airfoil surface. The trailing edge, in particular, represents a very challenging region to cool. A lot of turbine blade cooling involves internal cooling through convection. Due to the thin profile of the trailing edge, internal cooling is very challenging, and therefore film cooling is usually employed. Different forms of film cooling have been employed, such as pressure-side film cooling holes, trailing edge ejection, or slots, which are all compared in the study by Rehder [1].

Telisinghe [2] studied different trailing edge cooling configurations on a flat plate with an involute leading edge profile. One of the configurations tested is a machined cutback trailing edge with discrete film holes, such as the geometries in this study. A comparison of film effectiveness data from the machined cutback geometry with the current study is of relevance, despite some differences in the experimental facility. The geometries by Telisinghe [2] were tested on a flat plate facility (this study was done on a turbine blade with a concave pressure surface). The study by El-Hady et al. [3] argued that concave surfaces - such as the one upstream of the trailing edge region in the current study - develop secondary flows, namely Taylor-Gortler vortices, which destabilise the boundary layer and increase mixing. Furthermore, the study by Telisinghe [2] was carried out at a low free-stream Mach number of 0.3. The Mach number for modern turbine blades in the trailing edge is near 0.8, as explained in the review by Sieverding and Manna [4]. The study by Lutum et al. [5] studied the effect of free-stream Mach number on film effectiveness in cylindrical film holes. They found that the case with Ma = 0.8 showed significantly higher levels of film effectiveness than the case with Ma = 0.4.

There have been few studies on manufacturing tolerances in turbine blades, particularly experimental studies. Manufacturing offsets in fan-shaped holes between the diffuser and cylindrical sections have been studied by Haydt et al [6] and Kang et al. [7]. To the best of the authors' knowledge, there are no experimental studies on manufacturing variations in trailing edge film hole geometries. Bunker [8] developed a simplified flat plate model of a cooled airfoil to evaluate the effect of manufacturing variations on blade wall temperature. Variations in the diameter of film

cooling holes could reduce blade life by up to 33%. Other important factors such as length and pitch-to-diameter ratio as well as TE exit slot aspect ratio were identified. Heinze et al. [9] analysed 500 turbine blades with optical scanners and developed a parametric model using a probabilistic investigation in order to assess the effect of manufacturing variability on relevant aerodynamic quantities. Ultimately, probabilistic analysis can be used for more robust airfoil design. Kamenik et al. [10] studied samples of representative turbine blades using a 3D scanner and identified positional variations of trailing edge film cooling holes. The main finding from 3D scanning was that blade shape variations arise during manufacturing and are the main cause of film hole variation (as opposed to other reasons such as drill positioning).

The material capability of turbine blades allows for temperatures of up to 1100°C. However, it is generally understood that the blade life can be halved if the blade metal temperature prediction is off by 30°C, as explained in the study by Han [11]. It is therefore crucial for turbine blade manufacturers to understand how manufacturing tolerances in the trailing edge region affect film cooling effectiveness. The current study aims to add robustness to available data on film hole variations in the trailing edge cutback region which could occur during EDM processes. Film effectiveness measurements of design-intent and possible manufacturing variations were taken at engine representative blowing ratios (BR).

2 EXPERIMENTAL APPROACH

2.1 Test methodology

The experiments presented in this study were conducted in the high-velocity 2D linear cascade at the University of Oxford. The test section is a single-blade passage which follows the midspan streamlines of an engine-representative high pressure turbine blade. This allows for engine-representative Mach and Reynolds numbers. Perspex walls allow for full visual access of the blade and image data capture is performed using a BigEye CCD camera filtered to 610 $\pm$ 10 nm.

Figure 1a shows a view of the pressure surface and trailing edge of a test blade under UV lighting. The view is taken from the perspective of 'camera 2' as shown in the schematic in Fig. 1b

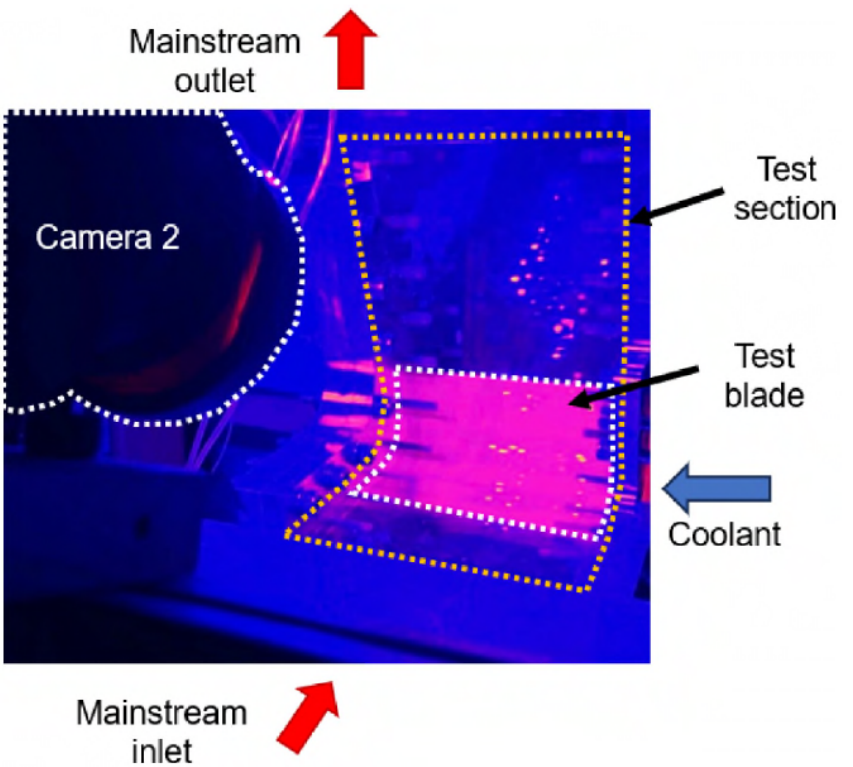

(a) View of test section under UV lighting

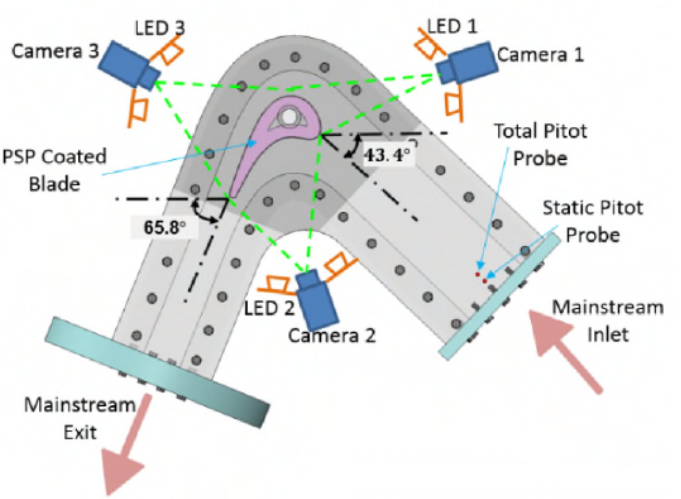

(b) Schematic of the test facility - Ngetich et al. [12]

Fig. 1: Test facility including (a) test section view under UV lighting and (b) schematic of test section by Ngetich et al. [12]

from the work by Ngetich et al. [12]. The pink dots in Fig. 1a on the perspex walls are reflections on the perspex from the UV LED lighting located above camera 2 (marked in Fig. 1a).

Mainstream air is fed from a 400 psi compressed air supply at ambient temperature. The compressed air is then passed through a regulator, followed by and orifice plate and lastly a honeycomb flow straightener. These steps are to ensure the correct mainstream flow conditions are achieved in the test section, after which the mainstream flow is exhausted to the atmosphere. Nitrogen is supplied from an oxygen-free 230 psi gas cylinder. Coolant air used in the PSP experiment is fed from a 100 psi reservoir. Both air and nitrogen are fed through long pipes to facilitate mixing before being fed into the plenum of the test blade. Further details on the operating conditions of the test facility can be found in the study by Ngetich et al. [12].

Test pieces were coated with a white primer of 80-100 μm to increase the signal captured by the cameras. Following that, five layers of UniFib PSP (single component PSP) were applied with an airbrush to ensure that the paint coat was thick enough for a sufficient signal. The relationship between a pressure reading from the PSP and the intensity reading is unique and can be found from a calibration curve. Calibration of a paint sample is performed in a separate calibration test facility, where a range of pressures and temperatures are applied and the corresponding coupon intensity is measured. PSP uses a mass transfer analogy that allows film cooling effectiveness to be defined as the ratio of mass fractions of a specific gas. These are converted to oxygen partial pressures using the ratio of molecular weights of the coolant and air. Film effectiveness can then be calculated using Equation 1.

$$\eta_f = 1 - \frac{1}{1 + \left[\frac{P_{O_2,air}/P_{O_2,ref}}{P_{O_2,c}/P_{O_2,ref}} - 1\right]\frac{W_c}{W_{air}}} \tag{1}$$

When Nitrogen is used as coolant, the ratio of molecular weights is approximately 1. During each experiment, 30 TIFF (tagged image file format) intensity images are captured for each condition to account for variance in the image data capture. These images were then averaged in

post-processing to give a mean intensity reading. Each experiment involves taking four intensity measurements: a reference intensity, a black intensity (to account for camera noise), an intensity with air as coolant and an intensity with nitrogen as coolant. The intensity measurements are then used to calculate film effectiveness using Equation 2.

$$\eta_f = 1 - \frac{(I_{ref} - I_b)/(I_{N_2} - I_b)}{(I_{ref} - I_b)/(I_{air} - I_b)} \tag{2}$$

Further details on the mechanism and measurement technique of PSP can be found in the well documented work by Han et al. [13]. A total pressure probe in the plenum of the test blades was used to measure the PR across the film holes, defined as the total coolant pressure over the local mainstream external static pressure ($\frac{p_{c,0}}{p_{\infty,s}}$). The external static pressure field around the blade was measured in a separate experiment which involved a test blade with multiple static pressure tappings. The test blades with manufacturing variations were tested for engine-representative blowing ratios between 0.6-1.1.

2.2 Geometries & Design parameters

The test blade has a uniform profile in the spanwise direction (shown in Fig. 2). Coolant is fed from the hub into a plenum with a uniform area and flow direction perpendicular to the mainstream flow. The blade wall thickness near the trailing edge was based on engine-representative wall thicknesses in order to keep representative values for the length of film cooling holes. The test pieces used in the current study were built using acrylic resin with a 3D Systems Multijet MJP 2500 Plus in-house printer. This provides a nearly adiabatic surface (thermal conductivity of = 0.12 W/m·K). A mean surface finish roughness of $Ra/D = 0.004$ was measured using an Alicona Infinite Focus 3D profilometer. The diameter of the film holes was measured through pin gauging as well as using a replication material with a resolution of $0.1\mu m$. An initial test piece revealed a shrinkage of 5-10 % of the film hole diameters after the part was printed and cured to remove printing support material. A correction was then applied to the blade designs in order to manufacture the intended

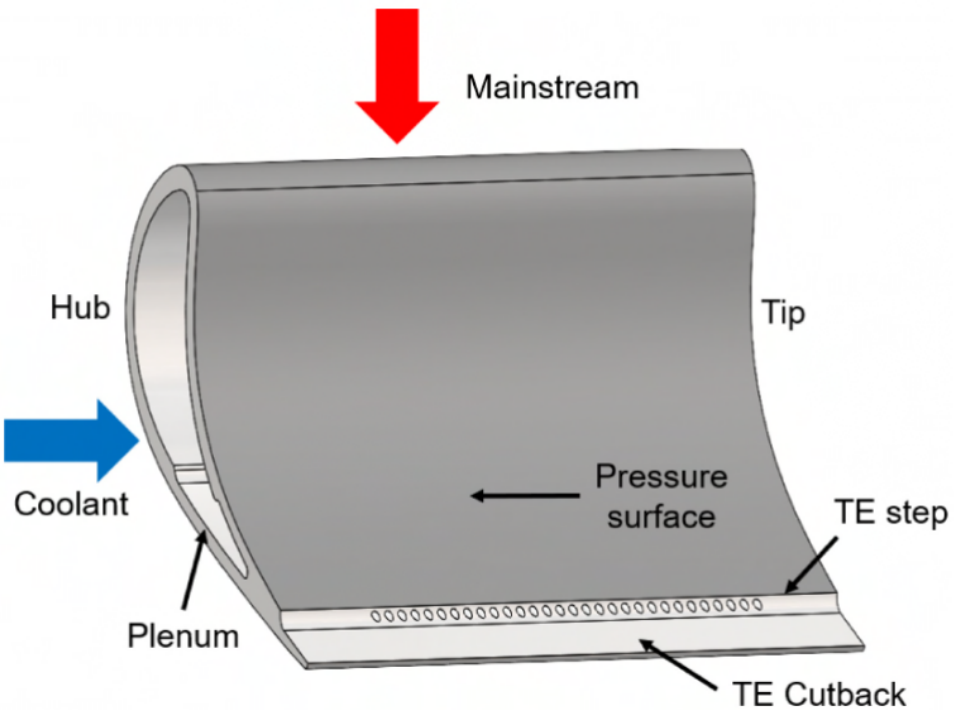

Fig. 2: Blade description

film hole diameter.

Figure 3 shows the definition of the baseline trailing edge cutback geometry. The cutback section is a flat surface measuring approximately 10D in the streamwise direction. Throughout the coolant channel, the film hole has a constant cross-section. The film hole axis is laterally inclined by 30° and exits on a plane parallel to the cutback surface (offset by 0.8D). The bottom part of Fig. 3 shows a top view of a film hole with an inclination angle of 30° in the spanwise direction. The definition of the film hole is the same for every test blade in this study. The trailing edge step is a sharp edge between the pressure surface and the machined cutback section (note that an inspection of the printed parts revealed a fillet at this edge measuring R/D = 0.2).

A combination of manufacturing variations in the trailing edge definition and film hole configurations is proposed here. The variations were gathered into three categories defined as V1, V2 and V3 in Fig. 4: a rounded step (V1), a hole shift (V2) and a step shift (V3). The Rounded step (RS) was created as a fillet in CAD with a radius of R/D = 0.5 (the baseline geometry is designed

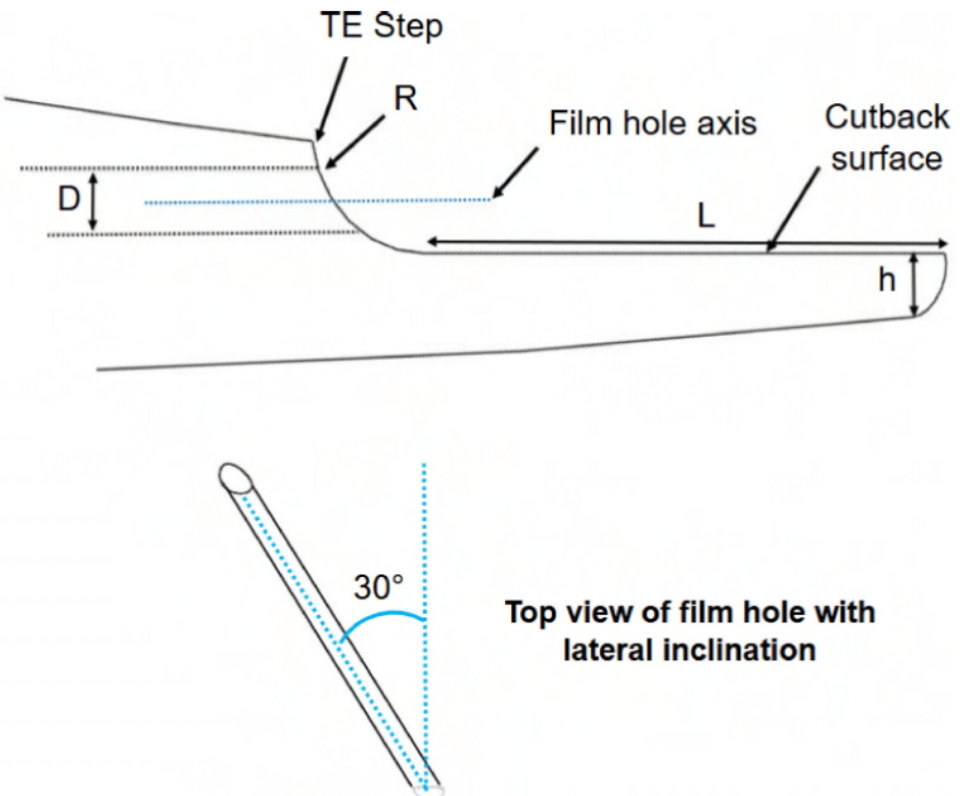

Fig. 3: Definition of the trailing edge for the baseline case

without a fillet). A hole shift refers to a shift in the axis of the film hole relative to the cutback surface, thereby changing the distance between the cutback surface and the film hole exit plane. A small hole shift (SHS) of 0.57D and a large hole shift (LHS) of 0.67D were tested (a positive shift refers to an upward shift, away from the cutback surface). Note that these cases led to the film holes breaking out upstream of the TE step, on the late pressure surface of the blade. Another hole shift case was tested with a shift of -0.8D. This case led to trenches in the cutback surface. A step shift refers to a change in the thickness of the cutback section while keeping the design-intent distance between the flat cutback section and the film hole plane. A positive step shift (PS) and negative step shift (NS) of 0.3D and -0.3D, respectively, were tested. Lastly two cases were tested with a combination of LHS and SHS hole shifts and NS step shifts, called LHS NS (Large hole shift & negative step shift) and SHS NS (Small hole shift & negative step shift). Both cases led to even larger distances between the cutback surface and the film hole axis.

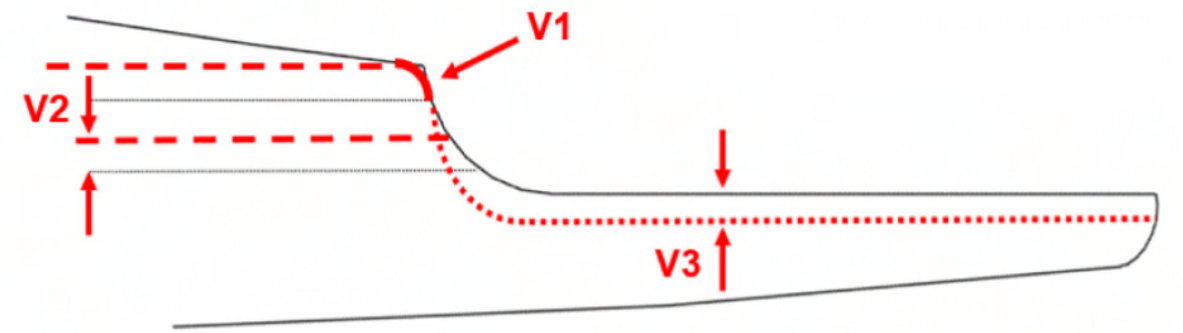

Fig. 4: Definition of the TE geometry for different permutation cases

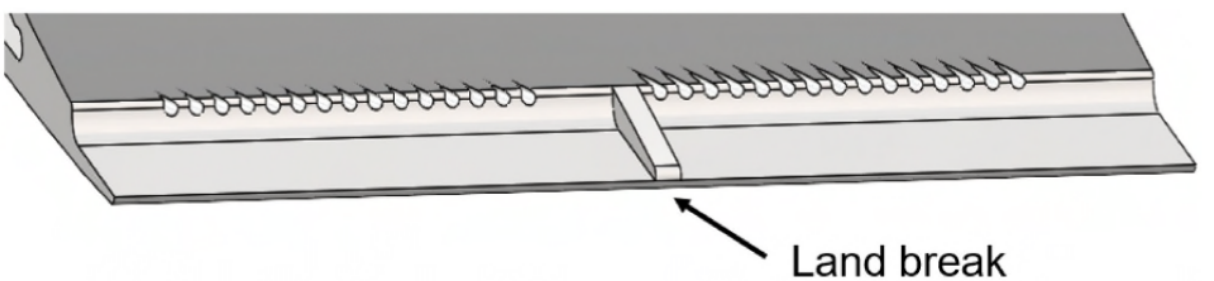

Fig. 5: Blade description for manufacturing deviations

Table 1 gives an overview of the different geometries tested, with different combinations of the geometry variations detailed above. For clarity purposes, the definitions V1, V2 & V3 used in Fig. 4 have been given. It should be noted that, except for the baseline, all test blades have the deviation V1. Five test blades were designed and tested, as shown in Table 1. These geometries are by no means exhaustive and other potential manufacturing variations can be tested. However, table 1 is intended to add to the understanding of robustness in trailing edge cutback film hole geometries. The baseline test blade has a row of 30 nominal film holes. The four remaining test blades were each designed with two separate manufacturing deviations, in order to save time and cost with the test campaign. As shown in Fig. 5, a land break was put in between the two different geometries in order to prevent coolant spillover from one geometry to another, which could potentially add uncertainty to the measurement of results. As will be shown later the land break was effective at preventing coolant spillover.

Table 1: Geometric dimensions of deviations tested

Test blade	Geometry	Denotation	Rounded Step (Y/N) (**V1**)	Hole shift (**V2**)	Step shift (**V3**)
1	Baseline	TE Base	N	-	-
2	Rounded step	RS	Y	-	-
	Wall impingement	Wall	Y	-0.8D	-
3	Small hole shift	SHS	Y	0.57D	-
	Large hole shift	LHS	Y	0.67D	-
4	Negative step shift	NS	Y	-	-0.3D
	Positive step shift	PS	Y	-	0.3D
5	Small hole shift & negative step	SHS NS	Y	0.57D	-0.3D
	Large hole shift & negative step	LHS NS	Y	0.67D	-0.3D

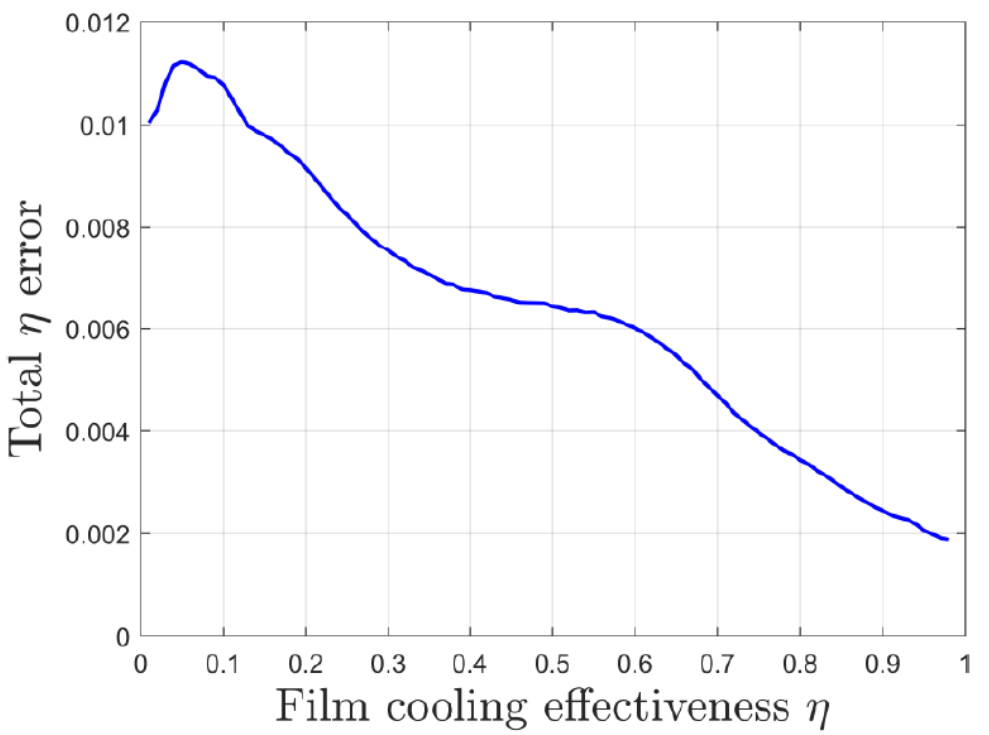

Fig. 6: Absolute uncertainty of UniFib PSP film effectiveness measurements

2.3 Measurement uncertainty

The two main sources in the PSP measurement are the uncertainty in the measured camera intensity as well as the temperature uncertainty. Han et al. [13] showed that PSP is highly sensitive to changes in temperature. These effects can be minimised if reference and test images

are taken at the same temperature. However, this proved to be quite difficult and even minor changes in temperature between test and reference cases can cause significant uncertainty in η_f. An estimation of the uncertainty due to temperature was made by using the perturbation method as described in the work by Moffat [14]. A perturbation of the temperature term was done across multiple datasets spanning the entire η_f range and averaging the uncertainty at each effectiveness value (to the nearest 0.01 η_f). The PSP uncertainty due to intensity for the test facility was quantified in the work by Wambersie [15]. In the current study, 30 images were taken for each case and averaged in order to minimise precision uncertainty of the data. Absolute values of η_f uncertainty are given in Fig. 6. The uncertainty of measured η_f is low at values of η_f close to 1, and high for η_f values close to 0. Note that the uncertainty refers to single data points and not averaged data. The reproducibility of experimental findings was previously shown by the authors [16]. The variation between five repeat tests of the same geometry was found to be just outside the analytical uncertainty in Fig. 6, however, all five repeat tests were within 0.01 η_f of the uncertainty range. The reason for this discrepancy could be other factors not included in the uncertainty calculation, such as PSP degradation.

The independent uncertainty measurements involved in the calculation of the blowing ratio are the following (all uncertainties reported represent a 95% confidence interval): pressure ($\pm$1000 Pa), temperature ($\pm$0.5 K), mass flow rate (0.8% of reading $\pm$ 0.2% of flow meter scale) and diameter measurement (pin gauging was used with a precision of 0.01 mm). Using the perturbation method described by Moffat [14], an uncertainty of 0.03 was found for a nominal BR of 0.74 for the baseline case. The uncertainties of independent measurements apply to all independent measurements during a test run.

2.4 Flow testing

Based on the theory of exhaust manifolds by Miller [17], it was assumed that a uniform flow distribution would be achieved since the holes were all fed from the same plenum. Note that this can be assumed if the branch loss ratio (cross-sectional area of all the holes divided by the cross-sectional area of the plenum) is less than 0.5. This ratio was calculated to be 0.14, and therefore below the theoretical limit.

To obtain the mass flow rate through individual geometries, flow tests were performed through separate experiments, as described in the study by Snyder et al. [18]. For every flow test one of the two geometries on each test blade was blocked off with a sealant and the mass flow rate through the seven middle film holes of each geometry was measured over a range of pressure ratios. A low mass-flow meter was used for this experiment, in order to reduce uncertainty in the mass flow measurement. Measured mass flow rates were then converted to a non-dimensional flow parameter (FP) to account for changes in gas pressure and temperature across tests. Based on the pressure ratio across the film holes, the flow parameter was used to calculate the mass flow rate through each geometry during PSP experiments. Knowing the mass flow rate, BR was calculated using Equation 3. Mean values of ρ_∞ and u_∞ were taken from every individual test run, while the area A was found from pin-gauging. While it is acknowledged that BR of individual holes might vary, this method allows for a comparison of mean BR across geometries.

$$BR = \frac{\rho_c u_c}{\rho_\infty u_\infty} = \frac{\dot{m}_c / A}{\rho_\infty u_\infty} \tag{3}$$

3 NUMERICAL METHOD

ANSYS Fluent 2023 R1 was used to perform steady Reynolds-Averaged Navier Stokes (RANS) simulations of the test cases. The two-equation shear stress transport (SST) $k-\omega$ model by Menter [19] was selected. ANSYS Fluent meshing was employed to generate a polyhedral mesh with prism layers, shown in Fig. 7. The fluid domain was created from a CAD of the experimental test facility. The test blade was then extracted from the fluid domain, leaving the solid parts of the test blade empty in the mesh. A part of the pipe (located outside of the test section) injecting coolant into the plenum of the blade was added to model the injection process correctly. Surface y^+ values in the region of interest (cutback and holes) were kept below 0.75 to be able to fully resolve the boundary layer.

A mesh independency study was performed to ensure that the mesh was sufficiently refined. The baseline geometry was modeled with different mesh sizes ranging from 3 to 41 million cells.

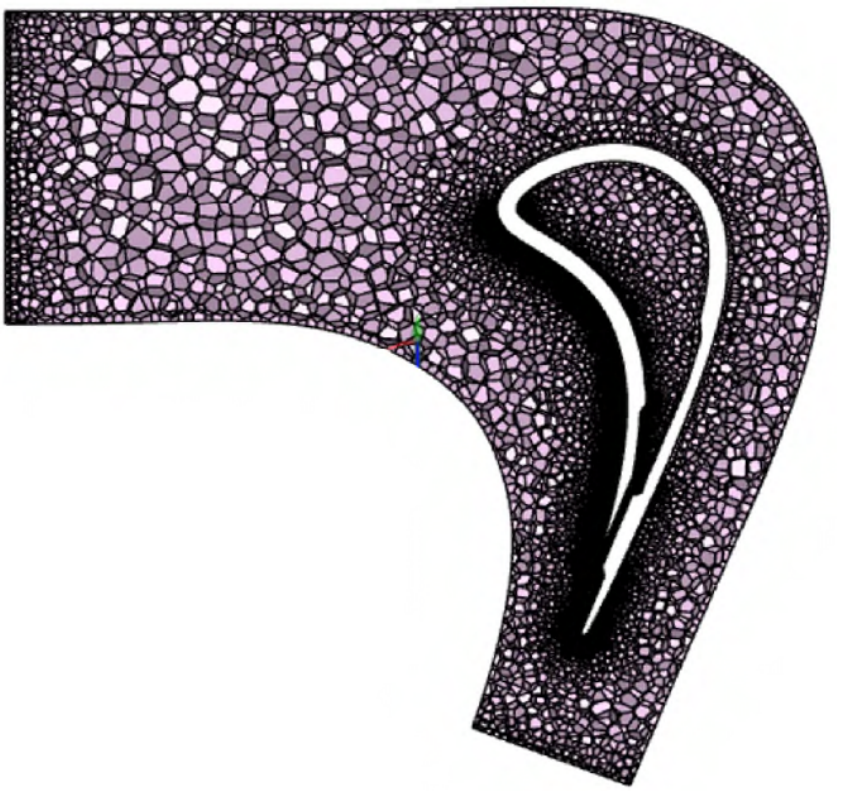

Fig. 7: View of mesh domain

Two measured quantities were used to judge mesh independency: area-averaged η_f in the cut-back region and the total coolant mass flow rate. Figure 8 shows the results of the mesh independency study (the y-axis has been normalised by the maximum area-averaged η_f value recorded). The residual area-averaged η_f and $\dot{m}$ errors for the 18 million cell mesh case are below 0.5% of the case with the highest number of cells. 18 million cells was therefore chosen for this study.

A pressure-based solver was employed with the coupled formulation, which enhances the stability of simulations, despite increasing the memory requirements. Gradients were evaluated using the least squares method and a second order flow discretisation scheme was applied to viscous and non-viscous fluxes using standard 2^{nd} order upwind. Convergence of the solutions was deemed when RMS residuals had decreased by at least two orders of magnitudes. When this was achieved, the mass flow imbalance was recorded at 0.002%.

All mainstream, coolant inlet and exit pressure, and temperature conditions were obtained from

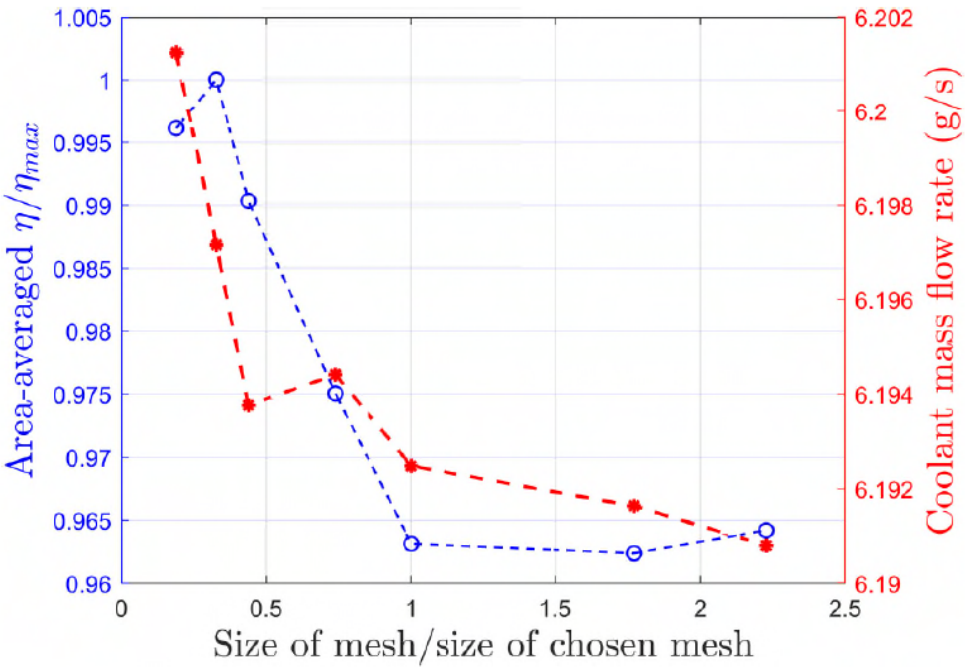

Fig. 8: Mesh independency study results

measurements during the experiments discussed in this study. An average of static pressure and temperature measurements was taken of the rig inlet conditions, while the total inlet pressure was taken from a traverse measurement in a separate experiment. The velocity direction of the coolant and mainstream were normal to the inlet surfaces in the mesh. Inlet turbulence was left at a default value of 5% with a length scale of 0.01 m, corresponding to the size of the flow-straightener hex mesh located upstream of the test section. The mainstream gas was set to air and the coolant was set to nitrogen to simulate the mass transfer analogy in PSP experiments. Adiabatic η_f was therefore quantified as N_2 species concentration on the surface of interest. Both air and nitrogen were treated as an ideal gas.

Jones et al. [20] performed a study on the usefulness of RANS in film cooling. They found that CFD overpredicted experimental film effectiveness results which was due to an underprediction of the mixing between the coolant and mainstream flow. This leads to underestimations of lateral and vertical dispersion of coolant flow. However, they found that velocity and thermal fields predictions of RANS within and above the film hole were in good agreement with experimental data. Additionally, it was found that general trends could be observed from RANS permitting a ”fast screening”

of hole designs. This suggests that RANS can be useful for industry and academics to an extent, when assessing the performance of film cooling holes. Another study by Jiang et al. [21] looked at mesh sensitivity of RANS simulations on film cooling flow. They found that mesh sizes with a medium size (of those simulated) was able to predict the experimental film effectiveness data relatively accurately. Especially when looking at the laterally averaged results, there was close agreement with the experimental features observed. Additionally, the effect of blowing ratio was captured by RANS. However, the mesh sizes used in the study by Jiang et al. [21] are much more refined and unfortunately not reproducible within the constraints of this study.

4 RESULTS AND DISCUSSION

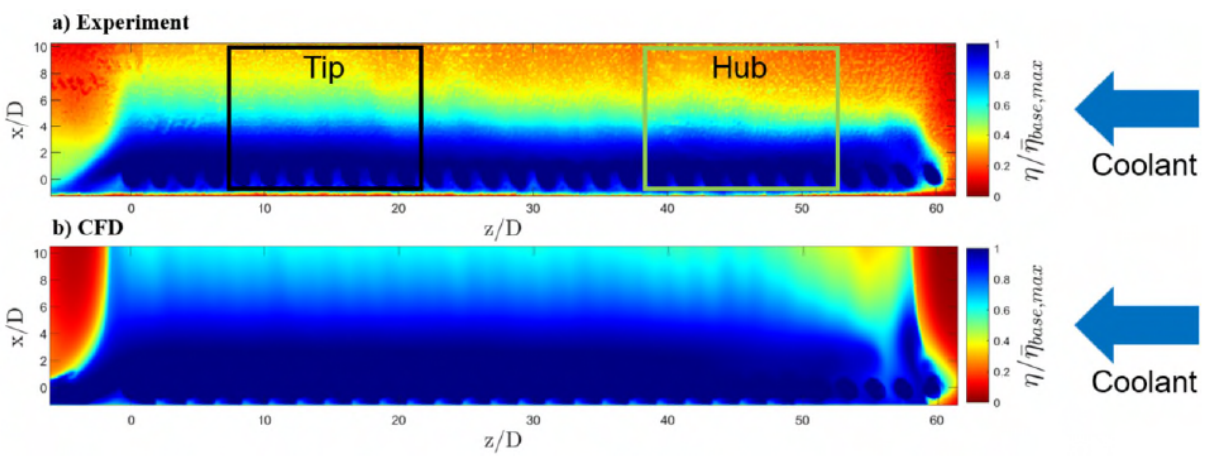

Fig. 9: Adiabatic film effectiveness distribution of the baseline geometry from a) experiment & b) CFD at BR = 0.61

In this section, the results from the experimental and numerical results will be analysed and discussed. The baseline geometry will be compared to the study by Telisinghe [2] in order to put this study into context. Unfortunately, no other studies with cutback geometries and discrete film cooling holes were found which could have formed the basis of a more thorough comparison. A comparison of geometries will first be done with film effectiveness contours. The analysis will then try to isolate certain locations in order to get a better understanding of how specific locations in the trailing edge are affected. CFD results will be compared with each other and used to inform

the flow fields that might lead to the experimental findings of the variations tested.

Note that all experimental contour plots and averaged plots have been normalised. The way this was done was to normalise calculated film effectiveness η_f by the maximum value of spanwise-averaged film effectiveness data $\eta_{f_{base,max}}$ from the baseline geometry.

4.1 Baseline geometry

Figure 9 shows contour plots of the baseline geometry for the experimental and numerical case at BR = 0.61. x/D = 0 was placed at the intersection of the film hole axis and the blade surface. The high η_f region ($\eta_f \geq 0.7$) for the experimental case extends to x/D = 4. The CFD case shows a much higher film effectiveness downstream of the holes, and the blue high effectiveness region extends beyond x/D = 6. An interesting feature in both the experimental and numerical results in Fig. 9 is the increase in high η_f contour extending further and further downstream for holes with smaller z/D (i.e. further away from the coolant feed side). This is the case for both the numerical and experimental case. While the coolant is fed through a plenum, it flows through a pipe before expanding into the plenum near the hub of the blade. This process could induce jetting and the effect of the plenum might not take place until the flow has traveled further to the tip. This could suggest that the internal cross flow is strongest near the hub (the right-most film hole in Fig. 9) and weakens as it expands into the plenum. The study by Gritsch [22] shows that at high internal cross flow velocities, the discharge coefficients are lower than for low cross flow velocity cases. This is because the high cross flow velocity case leads to low static pressures inside the coolant supply channel, and therefore doesn't provide a high enough pressure drop across the hole. A similar phenomenon was seen on the same test facility in another study by Wambersie et al. [23]. Transpiration panels tested on the pressure surface of a blade showed much higher film effectiveness levels towards the tip of the blade, suggesting they had received a higher mass flow rate than the film holes located near the hub of the blade.

Figure 10 compares spanwise average plots of the baseline geometry at BR $\sim$ 0.8 between the experimental and numerical case as well as the study by Telisinghe [2] of a machined cutback test plate. The experimental case was split into three different curves. Of the 30 film holes on the row, the average of the middle 14 film holes is shown by the red curve (denoted by 'Exp., BR = 0.82').

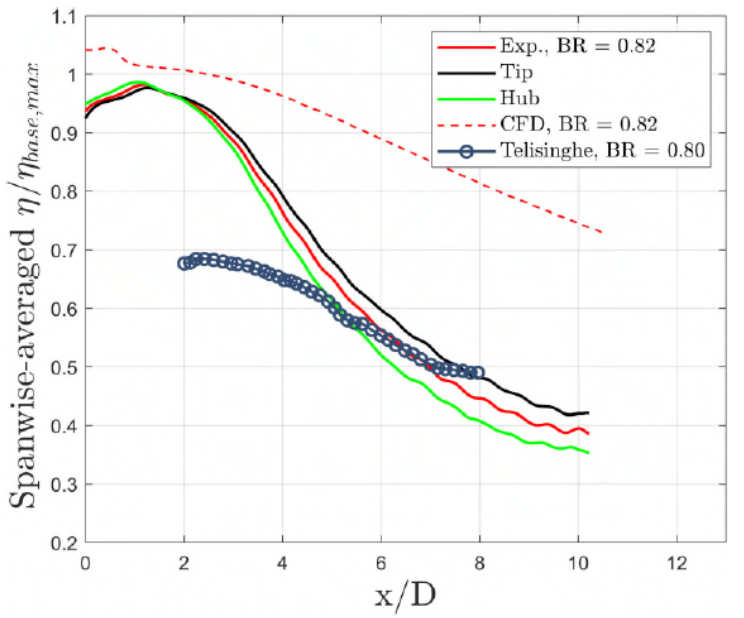

(a) Spanwise-average η_f at BR $\sim$ 0.8

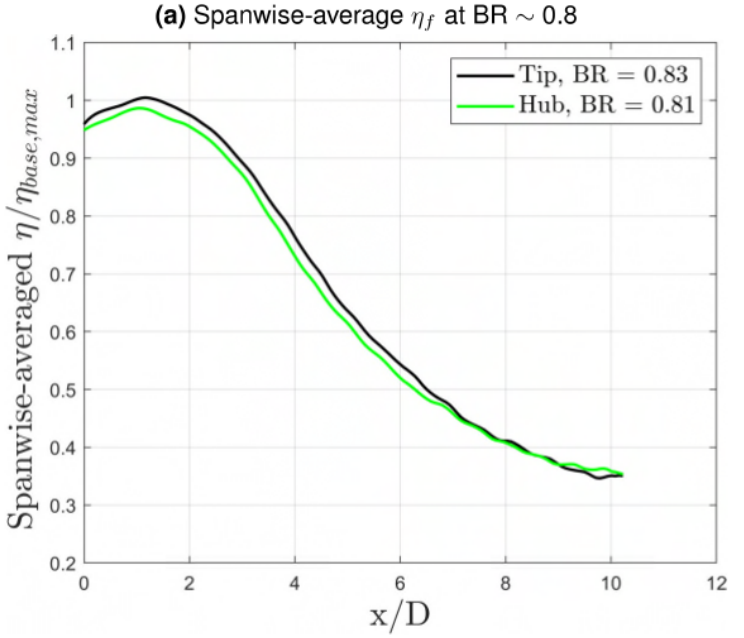

(b) Comparison of Tip and Hub film holes at BR $\sim$ 0.82

Fig. 10: Spanwise-average η_f of the baseline geometry at BR $\sim$ 0.8

The curves denoted by 'Tip and 'Hub' represent averages of the 7 film holes shown in the regions in Fig. 9 (the reason for this is that different geometries will later be analysed at these locations and therefore it is important to understand the difference in η_f). It is apparent from Fig. 10a that

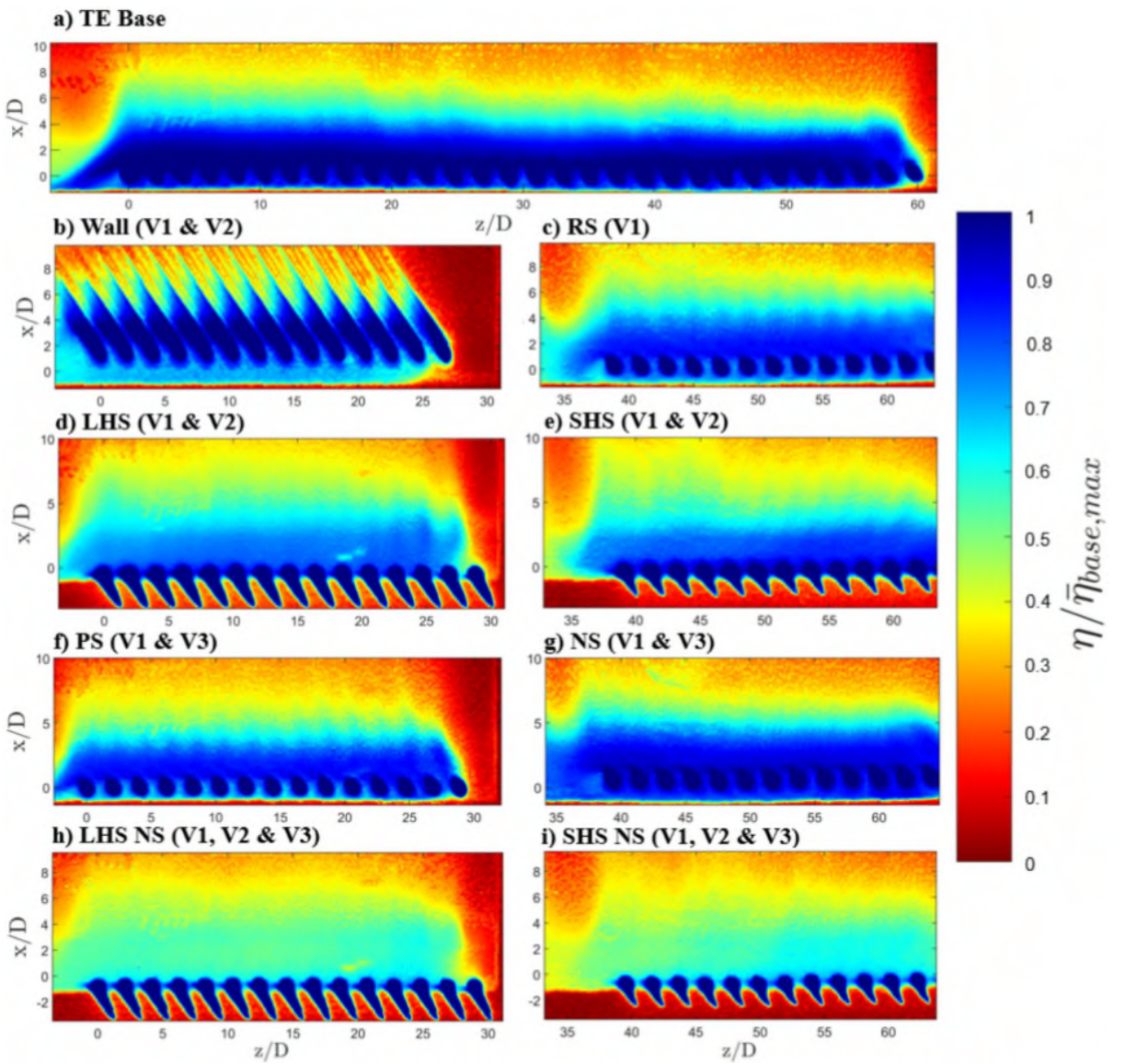

Fig. 11: Adiabatic film effectiveness distribution at BR $\sim$ 0.75

the tipwards located film holes perform significantly better than the hubwards located film holes by 6% at x/D = 4, and 7% at x/D = 9. However, they are taken from the same contour (i.e. at the same PR) and, as explained above, the discrepancy in η_f is most likely due to a higher discharge coefficient for film holes towards the tip. Indeed, during flow testing, geometries towards the tip were measured to have up to 7% higher mass flow rate at the same pressure ratio. Therefore, a better comparison between tip and hub film holes would be to look at test cases with similar

BR taken at different PR. Figure 10b compares the film holes at the tip and the hub at a BR $\sim$ 0.82 (taken at different PR). The tipwards located film holes still perform better than the hubwards located film holes though by much less: the tipwards film holes are better by 2% at x/D = 2, and less than 1% better at x/D = 9. The difference between the two curves in the near hole and mid-cutback region (up to x/D = 6) is slightly larger than the uncertainty of the data (see Fig. 6). The reason for this could be that the BR are not exactly matching or it could suggest that the difference in mass flow rate might not be the only factor contributing to the discrepancy. However, the trend is that tip- and hubwards film holes can be compared, if BR is matched (despite some uncertainty up to x/D = 6).

The CFD in Fig. 9b) shows a much higher η_f level than the baseline. In addition to having a higher level, the drop off is also less pronounced compared with the experimental case, highlighting that the numerical model struggles to simulate the mixing between the mainstream and the coolant. The data by Telisinghe [2] does not have the same initial level of η_f but doesn't drop off as much as the data from the current study. One explanation for this could be that the geometry in Telisinghe [2] does not represent a turbine blade such as the current study, but rather a flat plate with an involute leading edge profile. As explained in the study by El-Hady et al. [3], concave surfaces lead to unstable secondary flows which disrupt the boundary layer. This instability might lead to a faster decay of film effectiveness observed in the current study compared to that by Telisinghe. Another explanation might be the lower free stream Mach number in the experiment by Telisinghe [2] which has been shown to lead to lower film effectiveness levels in Lutum et al. [5].

4.2 Film effectiveness contours of manufacturing variation geometries

Figure 11 shows adiabatic η_f contours for all geometries with manufacturing variations at BR $\sim$ 0.75. Each row of geometries was tested on the same test blade. Additionally, the left column represents geometries which were located at the tip of the blade and the right column represents geometries located at the hub of the blade. Note that there is a land break between each geometry on the same test blade (shown earlier in Fig. 5). However, this was cut out in Fig. 11 to ease understanding of the results. The origin (0,0) was placed where the film hole axis of the baseline geometry cuts through the blade surface. The film holes in Fig. 11 are therefore slightly out of line

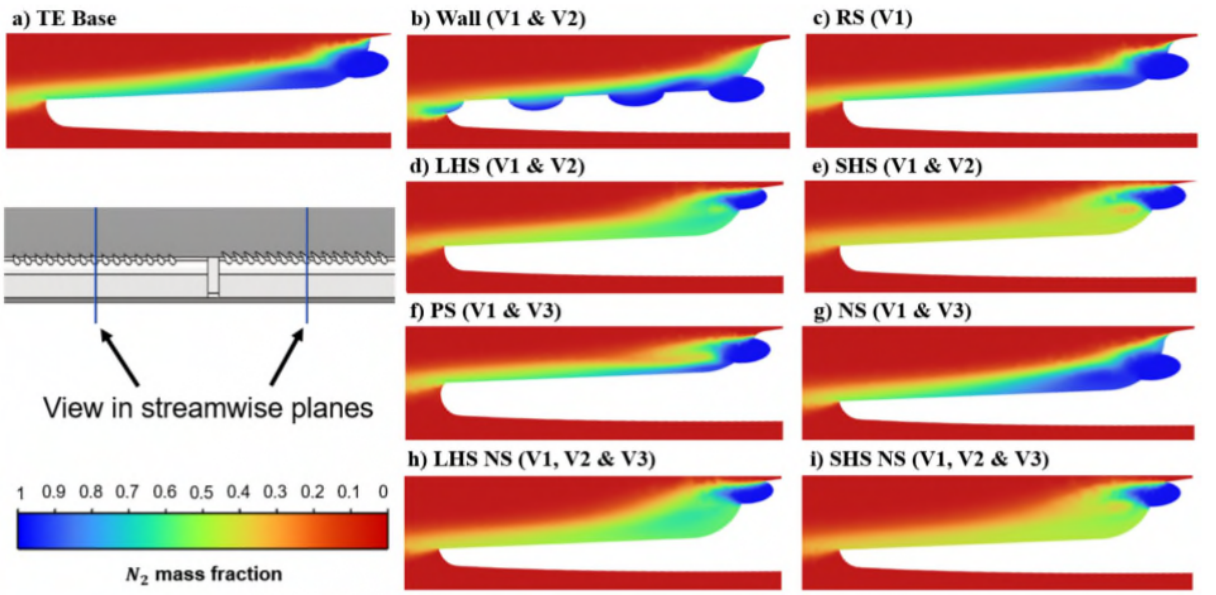

Fig. 12: CFD N_2 mass fraction contour plots in streamwise planes at BR $\sim$ 0.75

due to shifts in film hole axes.

The contours generally show good periodicity for each geometry, although some geometries show the same phenomenon as the baseline with better η_f to the left of the plot (near the tip). Note that during flow testing, geometries towards the tip of the blade were measured to have up to 7% higher mass flow rate than geometries at the hub. As explained earlier, the reason for this might be a stronger cross flow near the hub (to the right), which leads to lower discharge coefficients and lower mass flow rate.

4.2.1 Effect of a rounded step (V1)

The film effectiveness contour of the RS geometry (variation V1) in Fig. 11c) appears visually quite similar to the baseline geometry. However, the effectiveness values downstream of the film holes only reach values of $\eta_f = 0.8$ vs. values of $\eta_f = 0.9$ for the baseline. This is possibly due to the rounded step, which would facilitate mixing of the mainstream flow with the coolant further upstream than the baseline. Indeed, this can be seen in Fig. 12 which shows CFD N_2 mass fraction contour plots in the streamwise plane for each geometry at BR $\sim$ 0.75. Note that each streamwise plane was taken through the middle film hole, as shown with the CAD. A comparison of Fig. 12c)

with Fig. 12a) shows that the coolant layer immediately downstream of the RS geometry is slightly flatter and around 5-10% η_f lower than the baseline case. The flatter coolant layer suggests that the mainstream is mixing with the coolant layer further upstream than for the baseline geometry. Past x/D = 5, both contours have similar levels of η_f. Overall, the RS contour is more periodic with coolant streaks from each film hole visible. In contrast, the baseline geometry creates a smoother band and fills the cutback better.

4.2.2 Effect of a rounded step and hole shift (V1 & V2)

Three geometries were tested with a hole shift (V2) and a rounded step (V1). The Wall case in Fig. 11b) corresponds to a downward hole shift with half of the hole diameter cutting through the cutback surface and creating a trench for every film hole. This leads to a high η_f region of over 0.8 extending beyond x/D = 6 (though the film hole only exits at x/D = 1). The coolant appears to fill the trenches and hold the coolant near the surface further downstream. Figure 12b) supports this observation with high η_f values above 0.8 in the trenches, higher than the baseline case past x/D = 6. Comparing the Wall and RS case highlights the effect of the downward shift in the film hole axis (since both geometries have a rounded step). Indeed, it can be seen that the Wall case has a much higher local η_f between x/D = 1-5, which can be explained by the trenches as well as a close distance between film hole axis plane and cutback. The LHS and SHS cases correspond to upward shifts of the hole axis. Fig. 11d) & in Fig. 11e) show the film holes breaking out on the pressure surface further upstream than the baseline geometry. While η_f inside the holes is near 1, the region from x/D = 0 - 3 is closer to η_f between 0.7 - 0.8 vs. 0.8 - 0.9 for TE Base. LHS (Fig. 11d) performs slightly worse than SHS (Fig. 11e) which is likely due to a smaller distance between the film hole axis and the cutback surface. This possibly leads to better attachment of the coolant and less mixing with the mainstream. After x/D = 4, both LHS and SHS have similar η_f levels and decay after x/D = 9 below a value of η_f = 0.4. Interestingly, the CFD of LHS in Fig. 12d) predicts better attachment of the coolant than for SHS in Fig. 12e). A stronger recirculation region downstream of the film hole SHS appears to mix coolant and mainstream more than in the LHS case.

4.2.3 Effect of a rounded step and step shift (V1 & V3)

The geometries PS & NS were tested with a step shift (V3) and a rounded step (V1). Note that the step shift does not change the distance between the film hole axis plane and the cutback surface. Only the thickness of the cutback section is affected. The η_f contour for the NS in Fig. 11g) is up to 10% higher than the PS case from x/D = 0 - 7. Structurally, the coolant layer is more streaked for the PS case compared to the smoother band in NS. This suggests that the NS fills the cutback region better and mixes less with the mainstream flow. Figures 12f) and 12g) support these observations. Indeed, most of the coolant from the film of the PS case mixes out and only a fraction is attached to the cutback surface. In contrast, the NS case is much fuller in the y direction and η_f is 5 - 10% better than for the PS case.

4.2.4 Effect of a rounded step, hole shift and step shift (V1 & V2 & V3)

Lastly, the geometries LHS NS and SHS NS were tested with all variations of a rounded step (V1), hole shift (V2) and step shift (V3). These are shown in Fig. 11h) & Fig. 11i), respectively. An initial comparison with the LHS and SHS cases reveals the effect of the step shift. Indeed, the high η_f region over values of 0.7 is non-existent, suggesting that a critical threshold offset distance between film hole axis plane and cutback surface has been passed. Instead, this high η_f region has been replaced by a mid η_f region ($0.4 \leq \eta_f \leq 0.6$) which extends to x/D = 6 for both LHS NS and SHS NS. Towards the end of the trailing edge at x/D = 9, η_f drops to values between 0.2 and 0.3, 10% lower than the hole shift cases.

4.3 Spanwise-averaged film effectiveness

Figure 13 shows spanwise averaged η_f plots of all geometries and is intended to quantify observations made in Section 4.2. Spanwise-averaged plots were produced by averaging the middle 7 film holes for each geometry and dividing the dataset by the maximum spanwise-averaged η_f value of the baseline geometry at that BR. Figure 13a) reveals that the rounded step RS geometry is up to 10% worse than TE Base in the near-hole region (up to x/D = 3) and then recovers to similar η_f levels as TE Base (within 3 - 4 % η_f). Additionally, RS peaks just downstream of x/D = 0, while TE Base peaks just after x/D = 1. This plot suggests that the rounding of the trailing

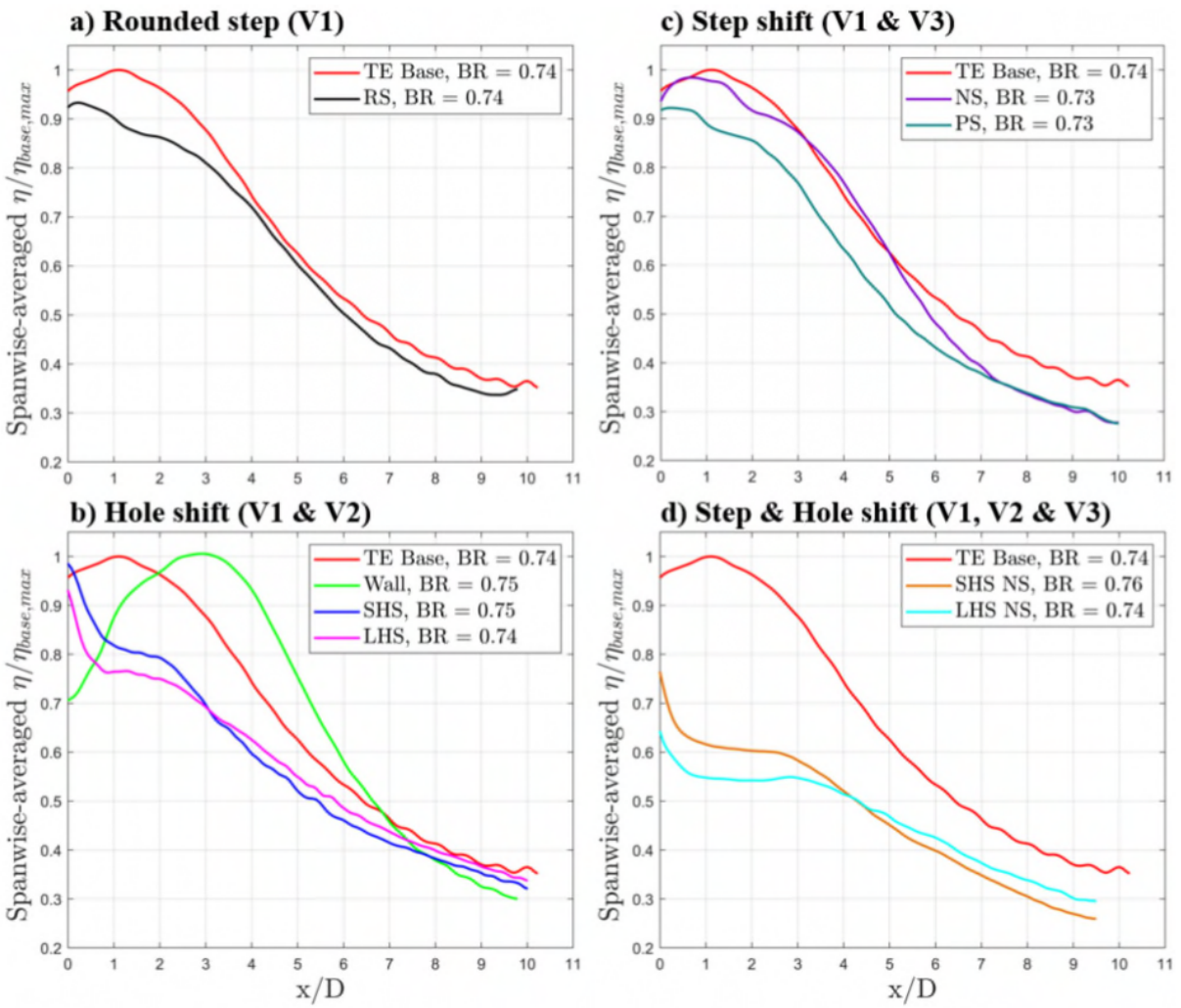

Fig. 13: Spanwise-average η_f of deviations at BR $\sim$ 0.75

edge step mostly affects the near-hole region by allowing the mainstream air to follow the rounded step and mixing with the coolant further upstream than the baseline trailing edge step with a sharp edge. Figure 13b) shows geometries with a hole shift. The Wall case peaks near x/D = 3 at the same value as TE Base but 2 film hole diameters further downstream. The region between x/D = 0 - 2 is 5 - 20% less cooled than TE Base. However, between x/D = 2 - 6, Wall outperforms TE Base by up to 20%. After that, the curve for Wall dips below that of TE Base with up to 5% lower η_f right at the trailing edge. The large hole shift LHS and small hole shift case SHS have similar curves, though in the near hole region (up to x/D = 3) SHS is up to 5% better and after that

LHS is marginally better by 2 - 3% η_f. Both cases peak much earlier than the baseline geometry (outside the plot limits) due to the vertical shift in the film hole axis. Between x/D = 1 - 3 TE Base is between 15 - 20% better than both hole shift cases, suggesting that the addition of a hole shift (V2) on top of a rounded step (V1) drops η_f by another 5 - 10%. Overall, a hole shift (V2) affects the near-hole and mid-cutback region most, but doesn't drop η_f in the trailing edge region more than the RS (V1).

Figure 13c) shows the effect of a step shift compared with the baseline. As noted earlier, a negative step shift NS almost has no effect on the near-hole region compared to TE Base (despite the addition of a rounded step V1), while after x/D = 5, NS starts to dip below TE Base and reaches a maximum drop of almost 10% after x/D = 7. In comparison, the positive step shift PS is almost 10% worse than NS up to x/D = 6, after which both cases converge. This suggests that NS only affects η_f in the late TE cutback region. In contrast, the PS is offset from TE Base over the entire cutback surface. Both cases peak between x/D = 0 - 1, just upstream of the baseline.

Figure 13d) shows the effect of adding a negative step shift NS to the cases with hole shifts LHS and SHS seen above in Fig. 13b). Offsetting the distance between the film hole axis plane and the cutback surface induces a larger drop in η_f as noted earlier in Fig. 11g) & Fig. 11h). In the near hole region up to x/D = 3, both LHS NS and SHS NS have more than 30% lower η_f than TE Base. After x/D = 6, both cases are within 7-10% of TE Base up until the trailing edge. Up to x/D = 3, SHS NS is up to 5% better and after that LHS NS is marginally better by 2 - 3% η_f. Note that this difference is just outside of the uncertainty band for the η_f value. Compared with Fig. 13b), the addition of V3 in the form of a negative step shift NS on top of V1 & V2, worsens η_f by 10 - 15% and by up to 10% in the mid-cutback and trailing edge region.

4.4 Performance of RANS CFD data against experimental data

This part of the study will compare the film effectiveness results from the experimental and CFD results at two locations: in the near-hole region at x/D = 2, and near the trailing edge at x/D = 9. The results are plotted against blowing ratio. The intent of this part of the study is twofold: first, to compare the experimental findings of the geometries, and understand where the geometries have the biggest effect compared to the baseline; second, to understand if the RANS

CFD results can be used as a way to inform on variations in film hole geometries in the trailing edge. Figures Fig. 14 & Fig. 15 have both been normalised by the peak baseline geometry η_f value from experimental results. This will also allow a comparison with CFD results.

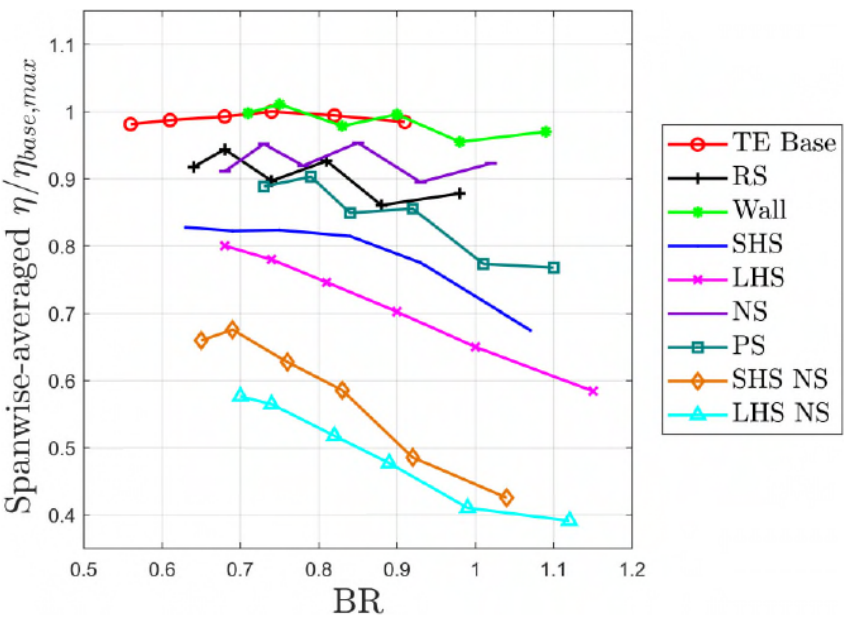

(a) Experimental η_f results at x/D = 2

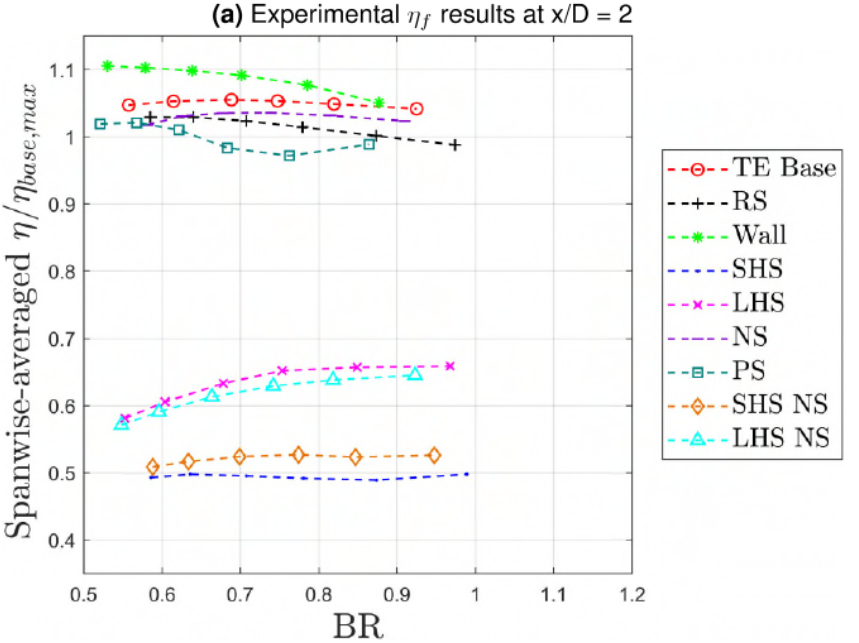

(b) CFD η_f results at x/D = 2

Fig. 14: Spanwise-averaged η_f at x/D = 2 of (a) experimental results and (b) CFD results

4.4.1 Effectiveness in the near hole region

Figure 14 shows spanwise-averaged η_f vs. BR at x/D = 2, just downstream of the film hole exit. This plot is intended to provide an even closer look at the performance of the geometries tested and give more data points at different BR. Overall, for the experimental results in Fig. 14a, it can be seen that the geometries are quite spread out over the η_f range and exhibit different behaviours depending on BR. The TE Base and Wall case have similar η_f at x/D = 2 and stay at a similar level of η_f over the range of BR tested between 0.6 and 1.1. The rounded step RS can be seen to have a detrimental effect with a 5 - 10% drop in η_f in the near hole region. This drop in η_f slightly increases with increasing BR. A change in cutback thickness through the addition of a step shift, drops η_f by 5-10% for NS compared to the TE Base. This represents the same drop in η_f as RS, suggesting that a negative step shift is not worse than the baseline on its own at x/D = 2. In contrast, PS shows a drop in η_f between 10 - 20%. Both NS and PS geometries have the same offset distance between film hole axis plane and cutback surface, though perform differently. This suggests that the location of the film hole axis plane in relation to the mainstream flow is a determining factor for η_f in the near hole region; a positive shift for PS (i.e. closer to the mainstream flow) leads to the coolant being ejected closer to the mainstream and likely mixes out without attaching as well as the NS geometry. A positive hole shift (i.e. SHS and LHS) decreases η_f even more in the near hole region and worsens with increasing BR. The further addition of a negative step shift on top of a rounded step and a hole shift (SHS NS & LHS NS) drops η_f values even more to the point where they reach less than 50% of TE Base η_f above BR = 0.9. Figure 14b shows CFD results at x/D = 2, normalised by the peak experimental baseline η_f. The numerical results are less spread out than the experimental ones, and, in contrast, can be grouped into two categories: the geometries with hole shifts (SHS, LHS, SHS NS $\&$ LHS NS) which have between 40 - 55% lower effectiveness than the other geometries (TE Base, RS, Wall, NS $\&$ PS). The baseline and Wall geometry are between 5 - 10% better than the experimental results. The geometries RS, NS and PS are 5 - 10% worse than the baseline CFD results, which corresponds to a 10 - 15% overestimation of experimental results. Additionally, the CFD results don't have the same drop off as experimental results at higher BR. The hole shift geometries LHS and SHS

underestimate experimental results by up to to 25%. While absolute levels of effectiveness are not well predicted, the CFD correctly predicts the order of the geometries for the 5 geometries TE Base, RS, Wall, NS and PS. This is not the case as soon as a hole shift is introduced. This might be explained by the higher distance between hole axis and cutback plane, which induces more mixing between coolant and mainstream.

There are several potential reasons for the differences observed between experimental and numerical results. As explained earlier in the study by Jones et al. [20], RANS generally underestimates the mixing between the coolant and the mainstream flow. This leads to underestimations of lateral and vertical dispersion of coolant flow and ultimately results in an overprediction of film effectiveness results. Another reason could be the turbulence model used for the current study. A study by Harrison and Bogard [24] simulated flat plate film cooling experiments with three different turbulence models - the realisable $k-\epsilon$, the standard $k-\omega$ and the RSM models. Varying results were found depending on the turbulence model employed. Additionally, the agreement between experimental and numerical results depended on whether centerline or laterally averaged film effectiveness was taken. Lastly, the aforementioned study by Jiang et al. [21] highlights the need for fine meshing in RANS simulations, which was unfortunately not possible for the current study.

4.4.2 Effectiveness near the trailing edge

Figure 15 shows spanwise-averaged η_f values at x/D = 9, right near the end of the trailing edge, representing one of the regions most difficult to cool on a turbine blade. Similarly to Fig. 14, this plot is intended to provide an even closer look at the performance of the geometries tested at a specific location.

At first glance, the geometries appear much closer together than at x/D = 2 in Fig. 14a, and all have a similar trend of increasing η_f with increasing BR. An explanation for this could be that the mainstream flow starts to dominate, and therefore the geometries are more forgiving, which is also supported by the CFD contour plots seen earlier in Fig. 12. Despite that, TE Base still outperforms all other geometries by 25% at lower BR and up to 35% at higher BR. As noted earlier, RS, SHS, and LHS have similar η_f values at lower BR, but start to dip below TE Base by up to 10% at higher BR. Both step shift cases PS and NS have very similar η_f values throughout the BR range, as

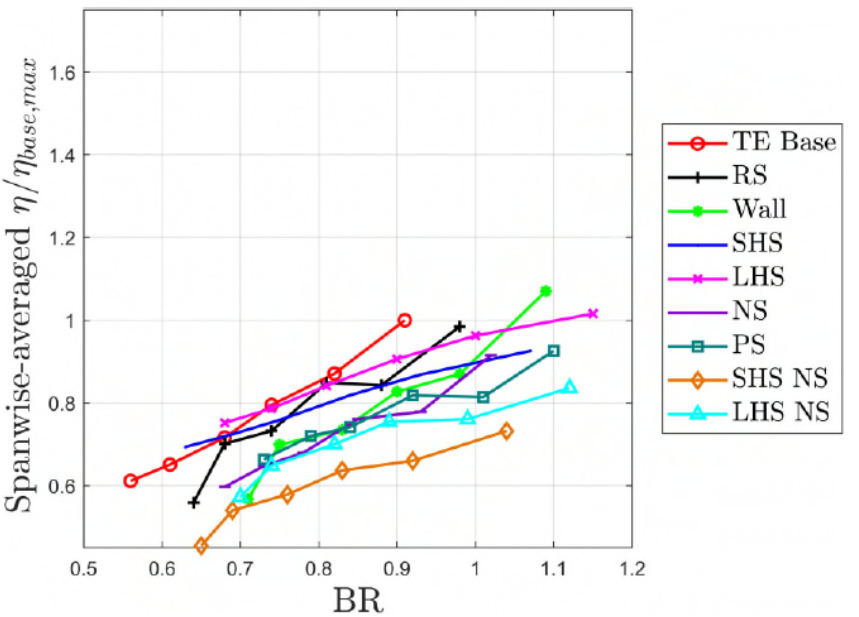

(a) Experimental η_f results at x/D = 9

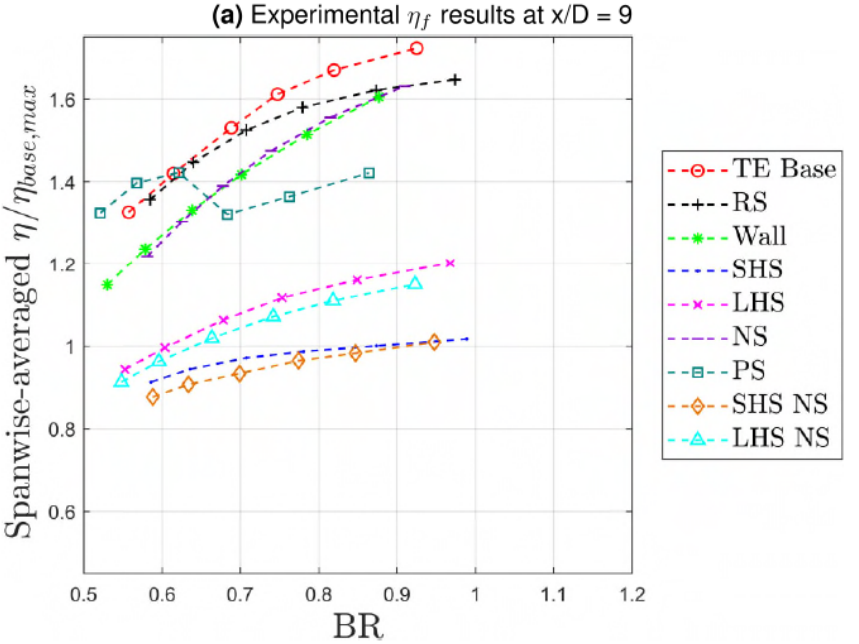

(b) CFD η_f results at x/D = 9

Fig. 15: Spanwise-averaged η_f at x/D = 9 of (a) experimental results and (b) CFD results

noted earlier in Fig. 13. The cases with step and hole shifts SHS NS and LHS NS are both the lowest in terms of η_f - between 25 - 35% below TE Base. LHS NS is slightly better than SHS NS by 5 - 10%. It appears that similar to Fig. 14, an increase in distance between the film hole axis

plane and the cutback surface leads to a higher drop in η_f. To put some of these discrepancies in film cooling effectiveness into the context of a real engine blade, a simple convection-cooled model from the study by Holland and Thake [25] was used to relate metal effectiveness ϵ_m to η_f, shown in Equation 4:

$$\epsilon_m = \frac{w_c^+ \eta_c + \eta_f(1-\eta_c)}{1 + (w_c^+ - \eta_f)\eta_c} \tag{4}$$

For an RB211 multipass blade that employs convection and film cooling, the values of cooling efficiency $\eta_c = 0.8$ and non-dimensional mass flow rate w_c^+ = 1.8 were used. For a decrease in film effectiveness η_f of 20% observed between TE Base and the PS or NS geometries at a blowing ratio of 0.9 in Fig. 14a, a drop in blade metal temperature of almost 30°C can be expected, based on Equation 4. From the study by Han [11], a difference in 30°C can halve the life of a turbine blade. In general, all manufacturing variations have a detrimental impact on film cooling effectiveness compared to the baseline geometry.

Comparing the CFD results in Fig. 15b with the experimental ones shows a larger spread between geometries. Furthermore, the absolute levels of η_f are significantly overpredicted: the baseline CFD geometry outperforms the experimental case by a factor of 1.7 at high BR. The SHS NS CFD geometry performs as well as the experimental TE Base case, highlighting the overprediction of CFD results at x/D = 9. However, the CFD again correctly predicts the order of the geometries (with the exception of SHS and LHS). TE Base performs the best, followed by RS, NS, Wall and PS (for BR $\geq$ 0.7). This is also the case for the experimental results. LHS NS is predicted 5 - 10% better than SHS NS, which is also the case for the experimental findings. Furthermore, the CFD correctly predicts the order of each geometries on each test blade (see Table 1). For instance, while SHS and LHS are not predicted in the correct order with respect to the other geometries, their relative order is correct - LHS is predicted to perform better than SHS.

Overall, the CFD results suggest that there is some benefit in using RANS in predicting the ranking of geometries. However, it is acknowledged that there are significant discrepancies be-

tween the absolute levels of predicted and measured film effectiveness.

5 CONCLUSION

Manufacturing variations were designed and tested to improve the understanding around the robustness and tolerances of film cooling in the trailing edge cutback region of a turbine blade. A steady RANS study was performed in ANSYS Fluent, and the results were used as explanations for the experimental results.

Overall, there are several takeaways from this work:

- Manufacturing variations underperform the baseline by up to 35% in the near-hole region and converge to within 10% η_f of the baseline geometry near the trailing edge.
- The rounded step allows the mainstream flow to penetrate into the coolant layer more easily than the sharp trailing edge step of the baseline geometry.
- A step shift performs differently depending on the direction of the shift. Therefore, the position of the film hole plane in relation to the mainstream matters and needs to be considered.
- A positive hole shift drops η_f by up to 20% (in the near hole region), suggesting that the distance between the film hole plane and the cutback surface is also a determining factor in the performance of the film cooling holes.
- The positive hole shift combined with a negative step shift drops η_f by another 10% over the entire cutback surface. Therefore, an increase in distance between the film hole plane and the cutback surface correlates with a decrease in η_f.
- RANS CFD results showed significant discrepancies between the predicted and measured film effectiveness results, but were able to predict the correct ranking of geometries for the most part.
- CFD results were also used to suggest explanations for how the manufacturing variations could affect the flow field and lead to the experimental results reported in this study.

ACKNOWLEDGEMENTS

The authors would like to thank the ongoing support provided by Rolls Royce PLC for this project. Additionally, we would like to thank Andreea Dabija, Liam Boland, Jason McCluskey and

Hal Surtell for the time invested in preparing test blades and experiments. We acknowledge the use of the University of Oxford Advanced Research Computing (ARC) facility.

REFERENCES

[1] Rehder, H.-J., 2012, "Investigation of Trailing Edge Cooling Concepts in a High Pressure Turbine Cascade—Aerodynamic Experiments and Loss Analysis," *Journal of Turbomachinery,* **134**(5), 09, p. 051029.

[2] Telisinghe, J., and Telisinghe, J., 2013, "Film cooling of turbine blade trailing edges," PhD thesis, University of Oxford.

[3] El-Hady, N. M., and Verma, A. K., 1984, "Instability of compressible boundary layers along curved walls with suction or cooling," *AIAA journal,* **22**(2), pp. 206–213.

[4] Sieverding, C., and Manna, M., 2020, "A review on turbine trailing edge flow," *International Journal of Turbomachinery, Propulsion and Power,* **5**(2), p. 10.

[5] Lutum, E., Von Wolfersdorf, J., Semmler, K., Naik, S., and Weigand, B., 2001, "Film cooling on a convex surface: influence of external pressure gradient and mach number on film cooling performance," *Heat and Mass Transfer,* **38**(1), pp. 7–16.

[6] Haydt, S., Lynch, S., and Lewis, S., 2017, "The effect of a meter-diffuser offset on shaped film cooling hole adiabatic effectiveness," *Journal of Turbomachinery,* **139**(9), p. 091012.

[7] Kang, Y. J., Park, S. H., Jeong, J. Y., Kim, G. M., and Kwak, J. S., 2022, "The effects of manufacturing tolerance on the film cooling effectiveness of a laidback fan-shaped hole," *Journal of Mechanical Science and Technology,* **36**(4), pp. 2127–2137.

[8] Bunker, R. S., 2009, "The effects of manufacturing tolerances on gas turbine cooling," *Journal of Turbomachinery,* **131**(4), 07, p. 041018.

[9] Heinze, K., Meyer, M., Scharfenstein, J., Voigt, M., and Vogeler, K., 2014, "A parametric model for probabilistic analysis of turbine blades considering real geometric effects," *CEAS Aeronautical Journal,* **5**, pp. 41–51.

[10] Kamenik, J., Toal, D. J., Keane, A., Högner, L., Meyer, M., and Shahpar, S., 2020, "Modeling and impact of high-pressure turbine blade trailing edge film cooling hole variations," In AIAA

Scitech 2020 Forum, p. 0905.

[11] Han, J.-C., 2018, "Advanced cooling in gas turbines 2016 max jakob memorial award paper," *Journal of Heat Transfer,* **140**(11), 07, p. 113001.

[12] Ngetich, G. C., Ireland, P. T., and Romero, E., 2019, "Study of film cooling effectiveness on a double-walled effusion-cooled turbine blade in a high-speed flow using pressure sensitive paint," In Turbo Expo: Power for Land, Sea, and Air, Vol. 58653, American Society of Mechanical Engineers, p. V05BT19A008.

[13] Han, J.-C., and Rallabandi, A., 2010, "Turbine blade film cooling using psp technique," *Frontiers in Heat and Mass Transfer (FHMT),* **1**(1), p. 013001.

[14] Moffat, R. J., 1988, "Describing the uncertainties in experimental results," *Experimental thermal and fluid science,* **1**(1), pp. 3–17.

[15] Wambersie, A., 2023, "High porosity cooling features for turbine blade applications," PhD thesis, University of Oxford.

[16] von Mueller, T., Bacci, D., Wambersie, A., Wong, T. H., Ireland, P., and Jackson, D., 2025, "Effect of blockages on film effectiveness on the pressure surface of a turbine blade," *Journal of Turbomachinery*, 01, pp. 1–40.

[17] Miller, D. S., 1978, *Internal flow systems.* Volume 5 of BHRA Fluid Engineering series. BHRA (Information Services).

[18] Snyder, J. C., and Thole, K. A., 2020, "Performance of public film cooling geometries produced through additive manufacturing," *Journal of Turbomachinery,* **142**(5), p. 051009.

[19] Menter, F. R., 1994, "Two-equation eddy-viscosity turbulence models for engineering applications," *AIAA journal,* **32**(8), pp. 1598–1605.

[20] Jones, F. B., Fox, D. W., and Bogard, D. G., 2019, "Evaluating the usefulness of rans in film cooling," In Turbo Expo: Power for Land, Sea, and Air, Vol. 58646, American Society of Mechanical Engineers, p. V05AT12A019.

[21] Jiang, Y., Murray, A., di Mare, L., and Ireland, P., 2022, "Mesh sensitivity of rans simulations on film cooling flow," *International Journal of Heat and Mass Transfer,* **182**, p. 121825.

[22] Gritsch, M., Schulz, A., and Wittig, S., 2001, "fefect of crossflows on the discharge coefficient

of film cooling holes with varying angles of inclination and orientation," *J. Turbomach.,* **123**(4), pp. 781–787.

[23] Wambersie, A., Wong, H., Ireland, P., and Mayo, I., 2021, "Experiments of transpiration cooling inspired panel cooling on a turbine blade yielding film effectiveness levels over 95," *International Journal of Turbomachinery, Propulsion and Power,* **6**(2).

[24] Harrison, K. L., and Bogard, D. G., 2008, "Comparison of rans turbulence models for prediction of film cooling performance," In Turbo Expo: Power for Land, Sea, and Air, Vol. 43147, pp. 1187–1196.

[25] Holland, M., and Thake, T., 1980, "Rotor blade cooling in high pressure turbines," *Journal of aircraft,* **17**(6), pp. 412–418.

LIST OF FIGURES

LIST OF TABLES

